The Journal of Chemical Physics

RESEARCH ARTICLE | JULY 25 2025

# Rotational envelope simulations in photodetachment spectroscopy: Precise measurement of electron affinity of NO and $O_2$

Wenru Jie ; Jiayi Chen; Rui Zhang ; Shuaiting Yan; Chuangang Ning



*J. Chem. Phys.* 163, 044309 (2025)
https://doi.org/10.1063/5.0284423









AIP Publishing

The Journal of Chemical Physics ARTICLE pubs.aip.org/aip/jcp

# Rotational envelope simulations in photodetachment spectroscopy: Precise measurement of electron affinity of NO and $O_2$

Cite as: J. Chem. Phys. 163, 044309 (2025); doi: 10.1063/5.0284423
Submitted: 8 June 2025 • Accepted: 3 July 2025 •
Published Online: 25 July 2025



Wenru Jie, Jiayi Chen, Rui Zhang, Shuaiting Yan, and Chuangang Ning[a)]

## AFFILIATIONS

Department of Physics, State Key Laboratory of Low Dimensional Quantum Physics, Frontier Science Center for Quantum Information, Tsinghua University, Beijing 100084, China

[a)]Author to whom correspondence should be addressed: ningcg@tsinghua.edu.cn

## ABSTRACT

The slow-electron velocity-map imaging (SEVI) technique can achieve accuracy better than 0.1 meV for atomic electron affinity (EA) determinations. However, molecular photoelectron energy spectra frequently exhibit complex rotational fine structures that induce substantial spectral congestions, thereby compromising the precision of molecular EA measurements. To obtain precise EA values of molecular species, we implement rotational envelope simulations of photoelectron energy spectra of molecular anions. Benchmark simulations for the well-characterized $OH^-$ successfully reproduce our cryogenic SEVI experimental spectra. Through application of this methodology to $NO^-$ and $O_2^-$, we establish EA(NO) = 0.029 24(46) eV and EA($O_2$) = 0.4477(10) eV, markedly enhancing the precision of these fundamental parameters compared to previous determinations.





## I. INTRODUCTION

Electron affinity (EA) is a fundamental parameter for understanding electronic structures and chemical reactivities of atoms and molecules. The EAs of various atoms have been measured with high precision, using techniques such as photoelectron energy spectroscopy (PES), laser photodetachment threshold (LPT), laser photodetachment microscopy (LPM), and slow-electron velocity-map imaging (SEVI).[1–5] A cryogenic SEVI (cryo-SEVI) apparatus in our laboratory routinely achieves uncertainty better than 0.1 meV for atomic EA.[4,6] Despite this high energy resolution, the accurate determination of molecular EAs continues to present substantial experimental challenges. For atoms, energy spectra usually exhibit very sharp peaks with a full width at half maximum (FWHM) of a few wavenumbers.[7–9] In contrast, molecular spectra display broadened peaks with complex profiles and FWHM values reaching a few tens or hundreds wavenumbers.[10,11] This spectral broadening arises because typical rotational level spacings are only a few wavenumbers or even less, which are too small to be resolved by most photoelectron instruments. As a result, each observed peak in a molecular photoelectron energy spectrum generally consists of numerous overlapping rotational transitions. The peak profile usually has a remarkable difference from a Gaussian peak, which causes the weighted center of the peak to systematically deviate from the true EA value. Consequently, the measurement uncertainty for molecular EAs is typically around 10 meV, significantly larger than that for atoms.[7]

Rotational envelope simulations were developed as a useful tool to address this issue. This approach was initially demonstrated by Hollas *et al.* to extract detailed information from the spectra of large molecules such as benzene derivative.[12] In 1973, Walker *et al.* extended this method to smaller molecules such as HF and DF, achieving excellent agreement between their simulations and experimental spectra while simultaneously determining ionization potentials of these molecules.[13] In subsequent years, Breyer *et al.* measured the EAs and molecular constants of OH, SH, and SD, with the EA uncertainties typically on the scale of tens of wavenumbers.[14] Schulz *et al.* were the first to provide a detailed derivation of the rotational transition line strength formula for the photodetachment of $OH^-$ and they successfully simulated the experimental spectra at a rotational temperature of 600 K.[15] More recently, Goldfarb *et al.* combined photodetachment microscopy experiments with

rotational envelope simulations to precisely determine the EA of OH with uncertainty of only 0.007 wavenumbers, and they also provided more accurate molecular constants.[16]

These hydrides have a large rotational constant $B$. For example, it is 18.5504 $cm^{-1}$ for OH at its vibrational ground state.[17] As a result, it is possible to directly resolve individual rotational peaks with the modern cryo-SEVI method,[18] thereby significantly enhancing the measurement accuracy. For the vast majority of molecules with typical rotational spacings of a few wavenumbers or even smaller, it is still a challenge to resolve the congested rotational transitions. In addition, the reported rotational simulations are all for the *s*-wave photodetachment. No rotational simulation for *p*-wave photodetachment has been reported.

In this work, we first validate the rotational envelope simulations by comparing it with the photoelectron energy spectra of $OH^-$, thereby demonstrating its validity and accuracy for the EA determination. Subsequently, we employ the cryo-SEVI method to obtain the photoelectron energy spectra of $NO^-$ and $O_2^-$. By comparing these experimental spectra with rotational envelope simulations, we achieve precise determinations of their EAs. This approach allows us to overcome the limitations imposed by rotational broadening and to set a new benchmark for the accurate measurement of molecular EAs.

## II. METHODS

### A. Experimental methods

The experiments were conducted on our cryo-SEVI apparatus, described in detail elsewhere.[4,8,18] In this work, the NO and $O_2$ anions were produced by expanding $N_2O$ gas (backing pressure ~3 bars) through a pulsed valve equipped with a high-voltage electron-gun ion source. The anions were directed through a radio frequency (RF) hexapole guide and then stored in a RF octupole ion trap for 45 ms. The ion trap was mounted on a cryogenically cold head held at 15 K and filled with buffer gas (20% $H_2$ + 80% He), allowing the anions to be cooled to their vibrational ground state through collisions with the buffer gas molecules. After cooling, the anions are extracted and mass-selected using a time-of-flight (TOF) mass spectrometer. The anions were then photodetached by an infrared laser, resulting in the production of photoelectrons and neutral molecules in different vibrational states. The infrared laser was generated through a nonlinear difference-frequency generation (DFG) process, involving a tunable dye laser and a 1064 nm laser beam. The two laser beams were combined within a nonlinear $LiNbO_3$ crystal, resulting in the emission of infrared light with a frequency corresponding to the difference between the 1064 nm and dye laser frequencies.[4]

The outgoing photoelectrons were accelerated by a non-uniform electric field within the imaging region and those with the same velocity formed a spherical shell. These photoelectrons were then projected onto a phosphor screen enhanced by microchannel plates (MCPs), with their positions captured by a charge-coupled device (CCD) camera in event-count mode. The resulting 2D projections were used to reconstruct the 3D velocity distributions using the maximum entropy velocity Legendre reconstruction (MEVELER) method.[19,20]

### B. General approach of rotational envelope simulations

To extract accurate EAs from the non-Gaussian peaks in photoelectron spectra for molecule anions, we conduct rotational envelope simulations to reproduce the experimental photoelectron energy spectra. Since the spectroscopic data for the final neutral molecules are usually well known, the EA measurement is not limited to the photodetachment channel with the neutral molecule at its electronic–vibrational ground state. The channel from the anionic ground state to a neutral excited state can also be adopted if accurate data for the energy levels of the neutral excited state are available. This option is critical for experiments of molecules with a very low EA value such as NO molecular.

The photodetachment process can be approximated as consisting of two steps, as shown in Fig. 1. In the first step, the anion absorbs a photon and is excited to a high-energy state known as the Rydberg state. In this state, the additional electron in the anion is bound so weakly that it can be approximated as a free electron. The total angular momentum $J_i$ of the intermediate state relates to that of anion $J''$, with transitions $J_i = J'' - 1$, $J''$, and $J'' + 1$ corresponding to the $P$, $Q$, and $R$ branches, respectively. Second, the anion undergoes dissociation, resulting in a molecule with total angular momentum of $J'$ and a free electron. Thus, the rotational transition intensity can be written as

$$I(J',J'') \propto \left| \sum_{J_i=J'\pm1/2} \langle u_\alpha, J' | u_i, J_i \rangle \langle u_i, J_i | r | u_\beta, J'' \rangle \right|^2 \propto \left| \sum_{J_i=J'\pm1/2} \langle u_\alpha, J' | u_i, J_i \rangle \langle u_i^e | r | u_\beta^e \rangle \langle u_i^v | u_\beta^v \rangle \langle u_i^r, J_i | u_\beta^r, J'' \rangle \right|^2, \quad (1)$$

where $u_\alpha$ represents the true wave function of neutral molecule, $u_i$ is the wave function of the intermediate Rydberg state, and $u_\beta$ denotes the true wave function of anion. Both $u_i$ and $u_\beta$ can be approximated as the product of three components: an electronic wave function $u^e$, a vibrational wave function $u^v$, and a rotational wave function $u^r$. The simulation thus requires calculating both the energy and relative intensity of all rotational transition channels, which are derived from the eigenvalues and eigenvectors of the Hamiltonian.

The first term of Eq. (1) shows the distinction between intermediate state and final states, which arises from the adoption of different perspectives on angular momentum coupling. In the intermediate state, the system is treated as a weakly bound anion, where the molecule and the loosely bound electron form a composite system described by $L$–$S$ coupling. In the final state, the neutral molecule and the free electron are considered as independent entities, whose angular momenta are coupled via $j$–$j$ coupling. This transformation between two coupling schemes can be formally expressed using the appropriate angular momentum projection coefficients, as detailed in Ref. 13 and Eq. (108.5–7) in Ref. 21,

$$\left| J'\Omega', \frac{1}{2} m_s \right\rangle = \sum_{\Omega_i} (-1)^{1/2-J_i+\Omega'} \sqrt{2J'+1} \frac{[(-1)^{s_i}]^{\delta\Omega',1/2}}{\sqrt{1+\delta_{\Omega_i,1}}} \times \begin{pmatrix} \frac{1}{2} & J_i & J' \\ m_s & \Omega_i & -\Omega' \end{pmatrix} | J_i S_i \Omega_i \rangle. \quad (2)$$

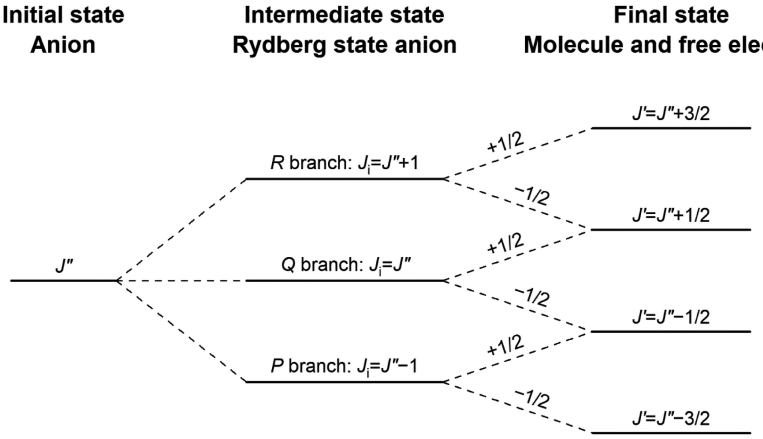


**FIG. 1.** Schematic illustration of the photodetachment process. It involves two steps: first, the anion absorbs a photon and transitions to a high-energy Rydberg state; second, transitions to a neutral molecule and a free electron.

The second term of Eq. (1) corresponds to the electronic transition dipole moment between the anion and the intermediate Rydberg state. The third term represents the vibrational overlap integral, which determines the vibrational transition strength and is commonly referred to as the Franck–Condon factor. The fourth term accounts for the rotational overlap and gives rise to the Hönl–London factor,[22] which depends on the anion's total angular momentum $J''$, its projection $\Lambda''$ of orbital angular momentum onto the molecular axis, and the change in orbital angular momentum projection $\Delta\Lambda = \Lambda_i - \Lambda''$.[23]

At this point, we can calculate the transition line intensity $I(E_b)$ for each rotational transition channel. To simulate the experimental spectrum, it is necessary to apply Gaussian broadening to each line intensity based on the instrument resolution and then sum them up to obtain the continuous simulated spectrum $I(BE)$. $BE$ is the binding energy.

Both the instrument resolution and the observed relative intensities depend on the kinetic energy. Our cryo-SEVI has a roughly constant width $\Delta r \sim 2$ pixels for the photoelectron spherical shell (radius $r$) photodetached from atomic anions. Since the kinetic energy of photoelectrons $E_k \propto r^2$, the spectrometer energy resolution $\Delta E$ for the transition with a binding energy $BE$ is given by

$$\Delta E \propto (h\nu - BE)^{1/2}. \tag{3}$$

Furthermore, the intensity is also subject to the Wigner threshold law near the threshold,[24]

$$I \propto (h\nu - BE)^{l+1/2}, \tag{4}$$

where $l$ is the angular momentum quantum number of the outgoing photoelectron, which results in a suppression of intensity in regions where the photoelectron kinetic energy is low.

### C. Application to OH, NO, and $O_2$ systems

Table I shows the initial, intermediate, and final states of OH, NO, and $O_2$. Since photodetaching OH and NO anions predominantly produces $s$ waves, the weakly bound electron occupies a $\sigma$-type Rydberg orbital, resulting in a $\Pi$-state Rydberg anion. However, due to the presence of two unpaired electrons, the spin configuration of the intermediate state may form a superposition of singlet ($^1\Pi$) and triplet ($^3\Pi$). Schulz *et al.*, in their study on OH rotational intensity simulations, assumed that for the majority of light molecules, spin–orbit coupling is negligible, thereby implying that the OH intermediate state predominantly exhibits only $^1\Pi$.[15] In our present work, both the $^3\Pi$ and $^1\Pi$ are considered. The eigenvalues and wave functions of the intermediate states are obtained by solving the Hamiltonian in the $^3\Pi$ and $^1\Pi$ representation. Since the highest occupied molecular orbital (HOMO) of $O_2^-$ is $\pi^*$ orbital, an atomic d-like orbital, photodetachment of $O_2$ anion yields a $p$ wave photoelectron near the threshold, placing the weak bound electron in a $\pi$-type Rydberg orbital and leading to an $^2\Pi$ intermediate state.

**TABLE I.** Initial, intermediate, and final states of photodetachment of $OH^-$, $NO^-$, and $O_2^-$.

| Species | Initial state | Intermediate state | Final state |
|---|---|---|---|
| $OH^-$ | $^1\Sigma$ | $^1\Pi$ | $^2\Pi$ |
| $NO^-$ | $^3\Sigma$ | $^1\Pi$ or $^3\Pi$ | $^2\Pi$ |
| $O_2^-$ | $^2\Pi$ | $^2\Pi$ | $^3\Sigma$ |

**TABLE II.** Matrix representation of $O_2^-$ anion and NO molecule Hamiltonian in the $^2\Pi$ basis.[a]

| | $^2\Pi_{1/2}$ | $^2\Pi_{3/2}$ |
|---|---|---|
| $^2\Pi_{1/2}$ | $-A/2 + B[J^2 + J - \frac{3}{4}]$ | $B\sqrt{(J-\frac{1}{2})(J+\frac{3}{2})}$ |
| $^2\Pi_{3/2}$ | $B\sqrt{(J-\frac{1}{2})(J+\frac{3}{2})}$ | $A/2 + B[J^2 + J - \frac{11}{4}]$ |

[a]From Eqs. (2) and (3) in Ref. 13, the same result was also obtained from Eqs. (1-17) and (1-18) in Ref. 25.

**TABLE III.** Matrix representation of $O_2$ molecule Hamiltonian in the $^3\Sigma$ basis.[a]

| | $^3\Sigma_{-1}$ | $^3\Sigma_0$ | $^3\Sigma_1$ |
|---|---|---|---|
| $^3\Sigma_{-1}$ | $BJ(J+1)$ | $-(B-\frac{1}{2}\gamma)[2J(J+1)]^{1/2}$ | 0 |
| $^3\Sigma_0$ | $-(B-\frac{1}{2}\gamma)[2J(J+1)]^{1/2}$ | $BJ(J+1)+2B-2\lambda$ | $-(B-\frac{1}{2}\gamma)[2J(J+1)]^{1/2}$ |
| $^3\Sigma_1$ | 0 | $-(B-\frac{1}{2}\gamma)[2J(J+1)]^{1/2}$ | $BJ(J+1)$ |

[a]From Eqs. (1-24) and (1-25) in Ref. 25.

**TABLE IV.** Matrix representation of NO Hamiltonian in the $^3\Pi$ and $^1\Pi$ basis.[a]

| | $^3\Pi_2$ | $^3\Pi_1$ | $^3\Pi_0$ | $^1\Pi_1$ |
|---|---|---|---|---|
| $^3\Pi_2$ | $A/2+B[J^2+J-4]$ | $B\sqrt{2(J+2)(J-1)}$ | 0 | 0 |
| $^3\Pi_1$ | $B\sqrt{2(J+2)(J-1)}$ | $BJ(J+1)$ | $B\sqrt{2J(J+1)}$ | $A/2$ |
| $^3\Pi_0$ | 0 | $B\sqrt{2J(J+1)}$ | $-A/2+BJ(J+1)$ | 0 |
| $^1\Pi_1$ | 0 | $A/2$ | 0 | $B[J^2+J-2]$ |

[a]From Table I in Ref. 13.

Simulations of the rotational envelope for OH have been previously derived in detail by Schulz *et al.*[15] and Goldfarb *et al.*[16] Accordingly, we focus on NO and $O_2$ for detailed derivation.

The relevant Hamiltonian matrix elements for the intermediate and final states are listed in Tables II–IV, corresponding to the $^2\Pi$, $^3\Sigma$, and mixture of $^1\Pi$, $^3\Pi$ basis representations, respectively. By solving the eigenenergy and eigenstates of these matrices, we can obtain the relative energy and wave functions of initial, intermediate, and final states of NO and $O_2$.

Due to spin–orbit coupling, the $^2\Pi$ state in both $O_2^-$ anion and NO molecule undergoes splitting into two states (mixed by $^2\Pi_{1/2}$ and $^2\Pi_{3/2}$), resulting in rotational level structures described by[14,25–27]

$$\begin{aligned}
^2\Pi_{1/2}: & B\left\{\left(J+\frac{1}{2}\right)^2-1-\frac{1}{2}\left[(2J+1)^2+Y(Y-4)\right]^{1/2}\right\} \\
& -D\left(J-\frac{1}{2}\right)^2\cdot\left(J+\frac{1}{2}\right)^2, \\
^2\Pi_{3/2}: & B\left\{\left(J+\frac{1}{2}\right)^2-1+\frac{1}{2}\left[(2J+1)^2+Y(Y-4)\right]^{1/2}\right\} \\
& -D\left(J+\frac{1}{2}\right)^2\cdot\left(J+\frac{3}{2}\right)^2.
\end{aligned} \tag{5}$$

Here, $B$ is the rotational constant, $D$ is the centrifugal distortion constant, and $Y$ is the ratio between the spin-orbital constant $A$ and $B$: $Y = A/B$. Note that the above-mentioned two states are mixed by $^2\Pi_{1/2}$ and $^2\Pi_{3/2}$. We label them using the leading term for simplicity. For $NO^-$ anion in its ground $^3\Sigma$ state, spin–orbit splitting can be considered negligible and its rotational energy levels can be approximated using the formula for the $^1\Sigma$ state,

$$BJ(J+1)-DJ^2(J+1)^2. \tag{6}$$

In contrast, the $^3\Sigma$ state of $O_2$ molecule exhibits noticeable fine structure splitting. Its three energy levels can be calculated by[25]

$$\begin{aligned}
^3\Sigma_0: & BJ(J+1)-DJ^2(J+1)^2, \\
^3\Sigma_{\pm1}: & BJ(J+1)-DJ^2(J+1)^2+(B-\lambda) \\
& \pm\left[\lambda^2-2B\lambda+B^2(2J+1)^2\right]^{1/2}\mp\gamma\left(J+\frac{1}{2}\right),
\end{aligned} \tag{7}$$

where λ quantifies the spin–spin interaction between the two unpaired electrons and γ describes the interaction between spin of the unpaired electron with the magnetic field generated by the molecule rotation.

As for the wave functions, for NO and $O_2^-$, the corresponding expressions are given in

$$\begin{aligned}
\text{NO}: & \begin{cases}
|u_\alpha, J'\rangle_{\text{NO}} = c_1\left|^2\Pi_{1/2}, J'\right\rangle + c_2\left|^2\Pi_{3/2}, J'\right\rangle, \\
|u_i, J_i\rangle_{\text{NO}} = \sum_{n=1}^{4} q_n\left(f_{1n}\left|^3\Pi_2, J_i\right\rangle + f_{2n}\left|^3\Pi_1, J_i\right\rangle + f_{3n}\left|^3\Pi_0, J_i\right\rangle + f_{4n}\left|^1\Pi_1, J_i\right\rangle\right), \\
|u_\beta, J''\rangle_{\text{NO}} = \left|^1\Sigma, J''\right\rangle,
\end{cases} \\
O_2^-: & \begin{cases}
|u_\alpha, J'\rangle_{O_2} = c_1\left|^2\Pi_{1/2}, J'\right\rangle + c_2\left|^2\Pi_{3/2}, J'\right\rangle, \\
|u_i, J_i\rangle_{O_2} = \sum_{m=1}^{2} q_m\left(c_{1m}\left|^2\Pi_{1/2}, J_i\right\rangle + c_{2m}\left|^2\Pi_{3/2}, J_i\right\rangle\right), \\
|u_\beta, J''\rangle_{O_2} = d_1\left|^3\Sigma_{-1}, J''\right\rangle + d_2\left|^3\Sigma_0, J''\right\rangle + d_3\left|^3\Sigma_1, J''\right\rangle.
\end{cases}
\end{aligned} \tag{8}$$

**TABLE V.** Conversion coefficients between $^2\Pi$ and the intermediate state $^3\Pi$ and $^1\Pi$.[a]

| $J'$, $\Omega'$ | $^3\Pi_2$ | $^3\Pi_1$ | $^3\Pi_0$ | $^1\Pi_1$ |
|---|---|---|---|---|
| $J_i+\frac{1}{2}, \frac{3}{2}$ | $\sqrt{\frac{J_i-1}{2J_i+1}}$ | $\sqrt{\frac{J_i+2}{2(2J_i+1)}}$ | 0 | $\sqrt{\frac{J_i+2}{2(2J_i+1)}}$ |
| $J_i+\frac{1}{2}, \frac{1}{2}$ | 0 | $\sqrt{\frac{J_i}{2(2J_i+1)}}$ | $\sqrt{\frac{J_i+1}{2J_i+1}}$ | $-\sqrt{\frac{J_i}{2(2J_i+1)}}$ |
| $J_i-\frac{1}{2}, \frac{3}{2}$ | $-\sqrt{\frac{J_i+2}{2J_i+1}}$ | $\sqrt{\frac{J_i-1}{2(2J_i+1)}}$ | 0 | $\sqrt{\frac{J_i-1}{2(2J_i+1)}}$ |
| $J_i-\frac{1}{2}, \frac{1}{2}$ | 0 | $-\sqrt{\frac{J_i+1}{2(2J_i+1)}}$ | $\sqrt{\frac{J_i}{2J_i+1}}$ | $\sqrt{\frac{J_i+1}{2(2J_i+1)}}$ |

[a]From Eq. (5) in Ref. 13.

**TABLE VI.** Conversion coefficients between $^3\Sigma$ and $^2\Pi$.

| $J'$, $\Omega'$ | $J_i-\frac{1}{2},1$ | $J_i+\frac{1}{2},1$ | $J_i-\frac{1}{2},0$ | $J_i+\frac{1}{2},0$ | $J_i-\frac{1}{2},-1$ | $J_i+\frac{1}{2},-1$ |
|---|---|---|---|---|---|---|
| $^2\Pi_{1/2}$ | $\sqrt{\frac{2J_i-1}{2(2J_i+1)}}$ | $\sqrt{\frac{2J_i+3}{2(2J_i+1)}}$ | 1 | 1 | 0 | 0 |
| $^2\Pi_{3/2}$ | $-\sqrt{\frac{2J_i+3}{2(2J_i+1)}}$ | $\sqrt{\frac{2J_i-1}{2(2J_i+1)}}$ | 0 | 0 | 0 | 0 |

As the intermediate and final states do not strictly conform to either Hund's case (a) or case (b), the actual wave functions are expressed as linear combinations of these basis states, with mixing coefficients $c$, $d$, and $f$. For the intermediate state, which is not a physically observable state, the mixing coefficients cannot be uniquely determined through quantum mechanical calculations alone. As such, $q_m$ and $q_n$ are treated as free parameters.

To evaluate the transition intensity term in Eq. (1), the angular momentum transformation coefficients between the intermediate and final states must be calculated. The relevant values for NO and $O_2$ are provided in **Note:** a) From Table 1 in Ref. 13.

In Tables V and VI, the Hönl–London factors are defined by the following equation: [23]

$$\mathrm{NO}^-:\begin{cases} I_R \propto J''+2, \\ I_Q \propto 2J''+1, \\ I_p \propto J''-1, \end{cases}$$

$$\mathrm{O_2}^-:\begin{cases} I_R \propto \dfrac{J''}{(J''+2)(J''+1)}, \\ I_Q \propto \dfrac{2J''+1}{J''(J''+1)}, \\ I_p \propto \dfrac{(J''-1)(J''+1)}{J''}. \end{cases} \tag{9}$$

This model provides a comprehensive framework for simulating molecular photoelectron energy spectra. It allows direct comparison with experimental data and serves as the foundation for extracting high-precision electron affinities in systems such as NO and $O_2$, as described in the following sections.

## III. RESULTS AND DISCUSSION

Figure 2 shows the photoelectron energy spectrum of $OH^-$ at 7.5 K at photon energy $h\nu$ = 14 959.21 $cm^{-1}$. The large rotational spacing of OH ensures that most peaks in the low-temperature spectrum correspond to a single rotational transition, as indicated

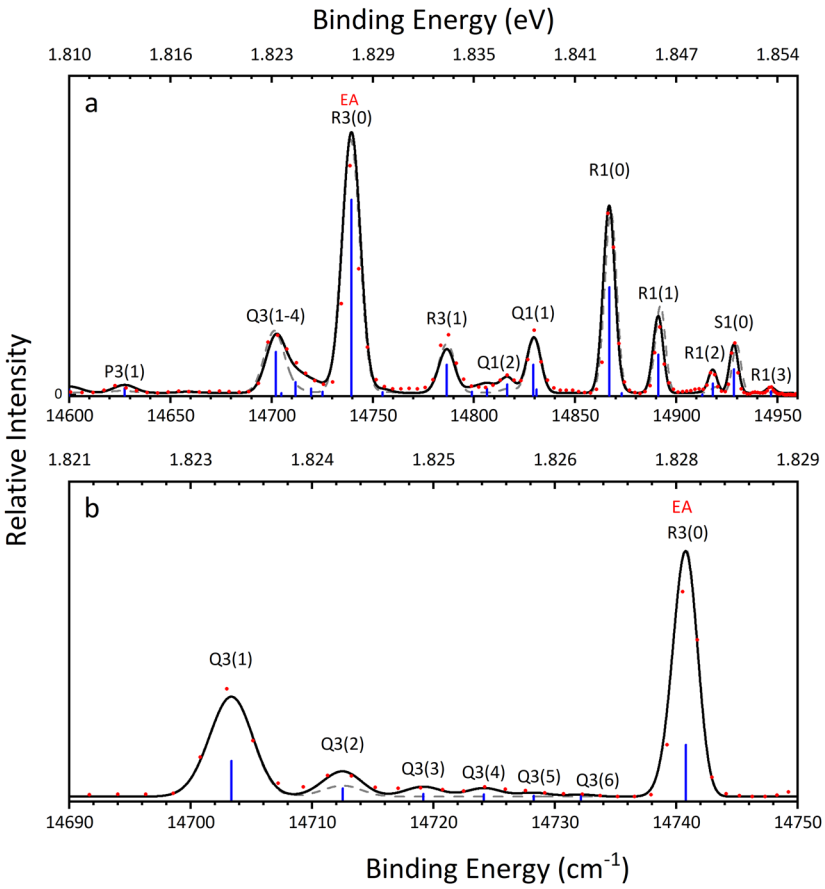


**FIG. 2.** (a) Comparison of experimental (red dots) and simulated (black curve) photoelectron energy spectra for $OH^-$ at $h\nu$ = 14 959.21 $cm^{-1}$. The blue vertical lines indicate individual rotational transition intensities. The black curve represents the total simulation incorporating Gaussian broadening with specified rotational population distribution of $OH^-$. The gray dashed line shows the simulation assuming Boltzmann distribution at 36 K. The *P*/*Q*/*R*/*S* branches denote $\Delta N$ = −1/0/+1/+2 transitions between anion and neutral states, respectively. The digit "1" after the letter in the label represents the $\Pi_{1/2}$ state, while "3" for the $\Pi_{3/2}$ of OH. The parenthetic number specifies the rotational quantum number ($N$) of $OH^-$. (b) Corresponding experimental and simulated spectra comparison at $h\nu$ = 14 759.65 $cm^{-1}$.

**TABLE VII.** Constants used in the rotational envelope simulation of $OH^-$. $A$ is the spin-orbital constant ($cm^{-1}$); $B$ is the rotational constant ($cm^{-1}$) for $v = 0$; and $D$ is centrifugal distortion constant ($cm^{-1}$).

| Species | $A$ | $B$ | $D$ |
|---|---|---|---|
| OH | −139.054[a] | 18.5504[b] | $19.38 \times 10^{-4}$[b] |
| $OH^-$ | | 18.7354[c] | $18.73 \times 10^{-4}$[c] |

[a]From Ref. 29.
[b]From Ref. 17. The relationship between the rotational constant in equilibrium position ($B_e$) and the rotational constant of a vibrational state ($B_v$) is $B_v = B_e + \alpha_e (v + 1/2)$, where $\alpha_e$ is the first-order correction coefficient to the rotational constant.
[c]From Ref. 16.

**TABLE VIII.** Rotational population coefficients of $OH^-$ anions (without multiplying the rotational degeneracy).

| Total angular momentum of anion ($J''$) | Boltzmann distribution coefficients (36 K) | Population distribution used in this work |
|---|---|---|
| 0 | 1 | 1 |
| 1 | 0.224 | 0.223 |
| 2 | 0.0113 | 0.0473 |
| 3 | $1.30 \times 10^{-4}$ | 0.0164 |
| 4 | $3.44 \times 10^{-7}$ | 0.0127 |
| 5 | $2.14 \times 10^{-10}$ | 0.0045 |
| 6 | $3.21 \times 10^{-14}$ | 0.0027 |

by the blue vertical spikes shown in Fig. 2. Meanwhile, Schulz *et al.* derived the formula for the rotational transition intensities of OH and successfully simulated the experimental spectrum at a rotational temperature of 600 K.[15] In addition, the diatomic constants of OH and its anion have been measured accurately.[16,28,29] These features make $OH^-$ an ideal system for verifying the rotational envelop simulation method.

To simulate the rotational envelope spectra, we first calculated the rotational transition line intensity using the formulas derived by Schulz *et al.* and broadened each line to a Gaussian peak. The molecular constants we used are listed in Table VII. As shown in Fig. 2(a), the experimental photoelectron energy spectrum of OH is in excellent agreement with the simulated spectrum. During the simulations, we observed that the population distribution of $OH^-$ on different rotational energy levels deviates significantly from the Boltzmann distribution. As presented in Table VIII, a direct comparison is made between the theoretical Boltzmann distribution coefficients at a rotational temperature of 36 K and the coefficients employed in our simulations based on the experimental spectrum. The experimental spectra reveal substantially higher population densities in higher rotational states than the prediction using the Boltzmann distribution. A similar trend was observed for the translational freedom of trapped ions in a RF ion trap.[30] The speed of trapped ions notably deviates from the Maxwell–Boltzmann distribution. The observed distribution in the high-speed region is significantly higher than the predictions using the Maxwell–Boltzmann distribution.

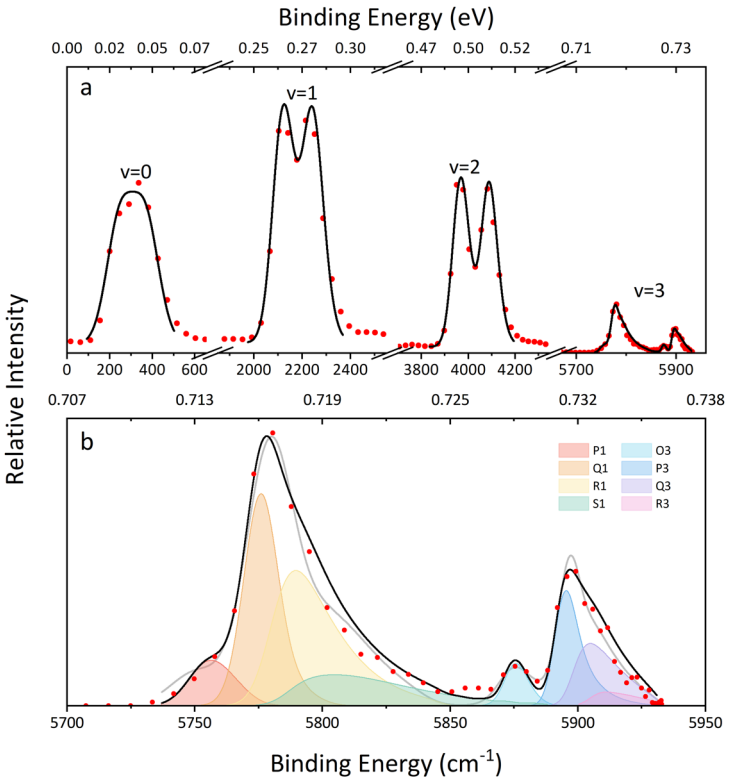


**FIG. 3.** (a) Comparison of experimental (red dots) and simulated (black curve) photoelectron spectra of $NO^-$ at $h\nu = 5932.81\ cm^{-1}$. (b) Magnified view of the $v = 3$ vibrational peak of NO. The black curve assumes a pure $^1\Pi$ intermediate state, while the gray curve accounts for a mixed $^1\Pi$ and $^3\Pi$ intermediate states. The *O*/*P*/*Q*/*R*/*S* branches denote $\Delta N = -2/-1/0/+1/+2$ transitions between anion and neutral states, respectively. The shaded curves represent branch-specific intensity summations across all anion rotational states. In addition, the digit "1" in the label represents the $\Pi_{1/2}$ state, while "3" for $\Pi_{3/2}$ of NO.

**TABLE IX.** Constants used in the rotational envelope simulation of $NO^-$.

| Species | $v$ | $A$ | $B$ | $D$ | Vibrational frequency ($cm^{-1}$, $R$ branch) |
|---|---|---|---|---|---|
| NO | 0 | 123.1336[a] | 1.696 28[b] | $5.385 \times 10^{-5}$[c] | 0 |
| | 1 | 122.8891[a] | 1.678 537[d] | $5.385 \times 10^{-5}$[c] | 1881.04[e] |
| | 2 | 122.6348[a] | 1.661 06[b] | $5.385 \times 10^{-5}$[c] | 3728.998[b] |
| | 3 | 122.3696[a] | 1.643 45[b] | $5.385 \times 10^{-5}$[c] | 5548.874[b] |
| $NO^-$ | 0 | | 1.44[f] | $1 \times 10^{-5}$[f] | |

[a]From Ref. 35.
[b]From Ref. 33.
[c]From Ref. 36.
[d]From Ref. 37.
[e]From Ref. 32.
[f]From simulations in this work.

Using this method, we obtained the electron affinity of OH as EA(OH) = 14 739.5(30) $cm^{-1}$ or 1.827 47(37) eV. The uncertainty primarily originates from the relatively large kinetic energy of photoelectrons. To improve the accuracy, the spectra can be acquired near the photodetachment threshold. For instance, Fig. 2(b) shows the photoelectron energy spectrum of OH at $h\nu$ = 14 759.65 $cm^{-1}$. From peak R3(0), we obtained EA(OH) = 14 740.79(25) $cm^{-1}$, which agrees well with the reported value of 14 741.02(3) $cm^{-1}$ by Smith *et al.* using the LPT method.[31]

The successful reproduction of the experimental spectra of $OH^-$ motivated us to conduct rotational envelope simulations for NO and $O_2$ using the same approach, attempting to accurately determine their EA values.

Figure 3 shows the photon energy spectrum of $NO^-$ at $h\nu$ = 5932.81 $cm^{-1}$. The final neutral NO molecules are in the ground state $^2\Pi$ with vibrational levels v = 0–3. The parameters in Table IX were used to simulate the four peaks corresponding to the transitions from the anionic vibrational ground state to the four neutral vibrational states. The neutral vibrational spacings precisely determined by previous infrared spectroscopy studies were used to construct the simulated spectra.[32,33] The intensity of each vibrational state and the rotational temperature were optimized for best fitting. The temperature for the best fitting is 120 K, significantly higher than the nominal temperature 15 K of the ion trap. The vibrational ground-state peak appears significantly broadened and lacks discernible fine structure due to limited resolution in the low binding energy region. However, in the higher binding energy region, the spin-orbital splitting of $^2\Pi$ is clearly observable.

Figure 3(b) shows an enlarged view of the $v$ = 3 vibrational peak of NO. The spin–orbit splitting of the molecular ground state $^2\Pi$ is

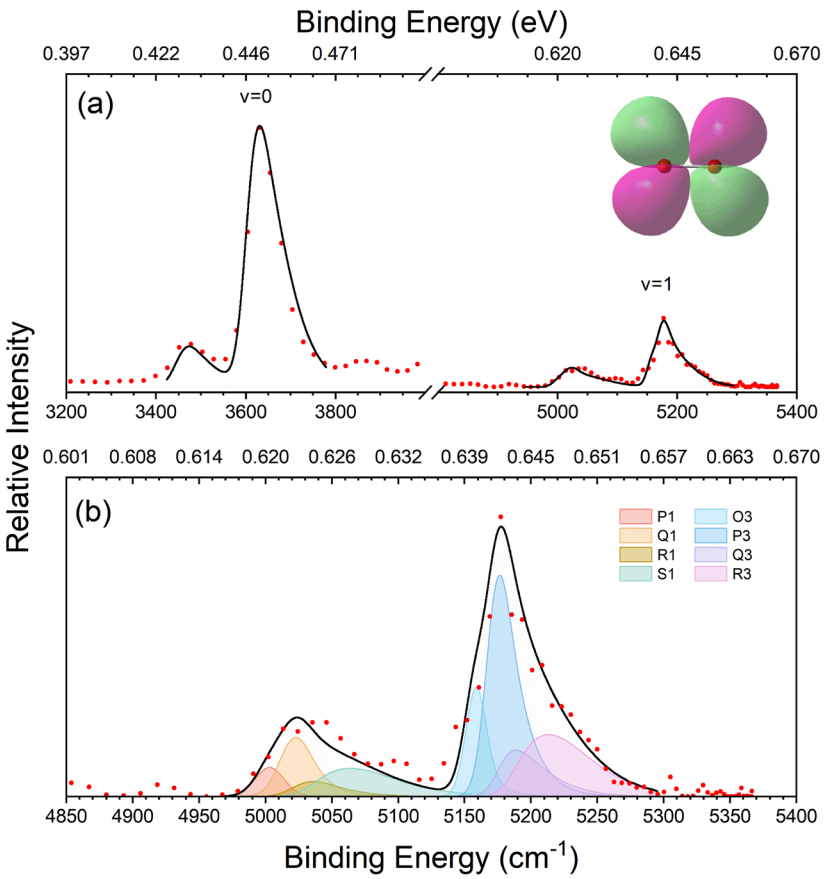


**FIG. 4.** (a) Comparison of experimental (red dots) and simulated (black curve) photoelectron spectra of $O_2^-$ at $h\nu$ = 5366.59 $cm^{-1}$. The inset shows the HOMO of $O_2^-$. (b) Magnified view of the v = 1 vibrational peak of $O_2$. The *O*/*P*/*Q*/*R*/*S* branches denote $\Delta N$ = −2/−1/0/+1/+2 transitions between anion and neutral states, respectively. The shaded curves represent branch-specific intensity summations across all anion rotational states. In addition, the digit "1" in the label represents the $\Pi_{1/2}$ state, while "3" for $\Pi_{3/2}$ of $O_2^-$.

**TABLE X.** Constants used in the rotational envelope simulation of $O_2^-$. λ is the spin–spin interaction between the two unpaired electrons ($cm^{-1}$), and γ describes the interaction between spin of the unpaired electron with the magnetic field generated by the molecule rotation ($cm^{-1}$). See Eq. (7).

| Species | $v$ | $A$ | $B$ | $D$ | λ | γ | Vibrational frequency ($cm^{-1}$, $Q$ branch) |
|---|---|---|---|---|---|---|---|
| $O_2$ | 0 | | 1.437 68[a] | $4.84 \times 10^{-6}$[b] | 1.9847[b] | −0.008 43[b] | 0 |
| | 1 | | 1.422[a] | $4.84 \times 10^{-6}$[b] | 1.9896[c] | −0.008 45[c] | 1556.352[d] |
| $O_2^-$ | 0 | −146[e] | 1.175[e] | $4.84 \times 10^{-6}$[b] | | | |

[a]From Ref. 36.
[b]From Ref. 38.
[c]From Ref. 39.
[d]From Ref. 40.
[e]From simulations in this work.

**TABLE XI.** Comparison of experimental and calculated EAs of NO.

| EA(NO) (eV) | Method | References |
|---|---|---|
| $0.024^{+10}_{-5}$ | PES | 41 |
| 0.026(5) | PES | 42 |
| 0.033(10) | TOF electron spectroscopy | 43 |
| 0.028 4(10) | Calculation | 44 |
| 0.029(2) | Calculation | 45 |
| 0.029 24(46) | Cryo-SEVI | This work |

**TABLE XII.** Comparison of experimental and calculated EAs of $O_2$.

| EA($O_2$) (eV) | Method | References |
|---|---|---|
| 0.43(3) | Analyses of the current waveforms | 46 |
| 0.46(5) | Measurements of the threshold for the charge exchange reaction | 47 |
| 0.451(7) | PES | 42 |
| 0.444(30) | PES | 48 |
| 0.448(6) | PES | 49 |
| 0.4477(10) | Cryo-SEVI | This work |

evident, with the fine structure of the $^2\Pi_{3/2}$ state clearly resolved. We compared rotational envelope simulations assuming different intermediate state configurations, which is either a pure $^1\Pi$ or a mixture of $^1\Pi$ and $^3\Pi$, and found that the resulting spectra are essentially consistent, as indicated by the black and gray curves shown in Fig. 3(b), respectively. The EA values simulated from these two intermediate states differ by only 0.12 $cm^{-1}$, supporting the validity of the $^1\Pi$ assumption for the intermediate state in light diatomic species such as NO.[15] When the intermediate state is $^1\Pi$, we determined EA (NO) to be 235.8(40) $cm^{-1}$ or 0.029 24(46) eV. As listed in Table XI, our result falls well within the error bars of previously reported values.

When $O_2^-$ was photodetached using a laser with energy of 5366.59 $cm^{-1}$, the products were free electrons and $O_2$ molecules in the neutral vibrational ground state and the first excited state. The corresponding spectra, shown in Fig. 4, were analyzed using the same rotational envelope simulation method with constants listed in Table X. The temperature used in simulation is 120 K. Near the photodetachment threshold, the photoelectron signals corresponding to the first vibrationally excited state ($v$ = 1) of $O_2$ decreases rapidly in intensity. As a result, the peak associated with this state has a very low count rate, and the experimental spectrum in this region appears noisy, introducing a relatively large uncertainty in the determination of the EA. This might be due to the fact that the highest occupied molecular orbital (HOMO) of $O_2^-$ is $\pi^*$ orbital, an atomic d-like orbital, and photodetachment of d-orbital usually has a very low photoelectron yield near the threshold.[34] Nevertheless, a decent spectrum was obtained by accumulating data for longer time at a relative larger kinetic energy. As shown in Fig. 4(b), the overall trend of the simulated spectrum agrees well with the experimental dots. Based on this analysis, the electron affinity of $O_2$ is determined to be EA ($O_2$) = 3611.0(80) $cm^{-1}$ or 0.4477 (10) eV. This result shows good consistency with previously reported values, as summarized in Table XII.

These results underscore the effectiveness of combining high-resolution photoelectron spectroscopy with rotational envelope simulations. This approach significantly improves the precision of EA measurements, particularly for systems where rotational fine structures cannot be resolved. It should be pointed out that the temperature used in the simulation is substantially higher than the nominal temperature of the cryogenically cold ion trap, which might be due to the leak of hot carrier gas from the ion source chamber into the ion trap and the possible RF heating of the ion trap, which is more significant for molecular anions with lower mass.

Beyond NO and $O_2$, this framework can be readily extended to other molecular anions by simply adapting the relevant Hamiltonians and rotational constants in Eq. (1), making it a versatile tool for high-accuracy spectroscopic analysis. Moreover, higher-resolution experimental spectra naturally lead to more accurate EA values and molecular constants, further enhancing the reliability of this approach.

## IV. CONCLUSION

In this study, we combined cryo-SEVI with rotational envelope simulations to achieve precise measurements of the EAs of NO and

$O_2$. The benchmark case of $OH^-$ verified the validity of the simulation method. The EA value of OH yielded through the rotationally resolved cryo-SEVI spectra is in excellent agreement with prior high-resolution studies. For NO and $O_2$, we obtained more accurate EA values: EA(NO) = 235.8(40) $cm^{-1}$ or 0.029 24(46) eV and EA($O_2$) = 3611.0(80) $cm^{-1}$ or 0.4477(10) eV. This work demonstrates that high-resolution cryo-SEVI spectroscopy joint with rotational analysis provides a powerful approach for determining molecular EAs. The methodology is applicable to a wide range of molecular anions.

## ACKNOWLEDGMENTS

This work was supported by the National Natural Science Foundation of China (NSFC) (Grant Nos. 12374244 and 12341401).

## AUTHOR DECLARATIONS

### Conflict of Interest

The authors have no conflicts to disclose.

### Author Contributions

W.J. and J.C. contributed to the design and implementation of the research, W.J. and J.C. to the analysis of the results, R.Z., S.Y. to the implementation and data analysis (support). C.N. supervised the project. W.J. and C.N. wrote and reviewed the manuscript.

**Wenru Jie**: Formal analysis (equal); Investigation (supporting). **Jiayi Chen**: Formal analysis (equal); Investigation (supporting). **Rui Zhang**: Investigation (supporting). **Shuaiting Yan**: Investigation (supporting). **Chuangang Ning**: Conceptualization (lead); Formal analysis (equal); Funding acquisition (lead); Investigation (equal); Writing – review & editing (equal).

## DATA AVAILABILITY

The data that support the findings of this study are available within the article.

## REFERENCES

[1] H. Hotop and W. C. Lineberger, J. Phys. Chem. Ref. Data **4**, 539 (1975).
[2] H. Hotop and W. C. Lineberger, J. Phys. Chem. Ref. Data **14**, 731 (1985).
[3] T. Andersen, H. K. Haugen, and H. Hotop, J. Phys. Chem. Ref. Data **28**, 1511 (1999).
[4] C. Ning and Y. Lu, J. Phys. Chem. Ref. Data **51**, 021502 (2022).
[5] J. C. Rienstra-Kiracofe, G. S. Tschumper, H. F. Schaefer, S. Nandi, and G. B. Ellison, Chem. Rev. **102**, 231 (2002).
[6] S. Yan, Y. Lu, R. Zhang, and C. Ning, Chin. J. Chem. Phys. **37**, 1 (2024).
[7] R. Tang, R. Si, Z. Fei, X. Fu, Y. Lu, T. Brage, H. Liu, C. Chen, and C. Ning, Phys. Rev. Lett. **123**, 203002 (2019).
[8] Y. Lu, R. Zhang, C. Song, C. Chen, R. Si, and C. Ning, Chin. Phys. Lett. **40**, 093101 (2023).
[9] R. Zhang, Y. Lu, R. Tang, and C. Ning, J. Chem. Phys. **158**, 084303 (2023).
[10] S. Yan, R. Zhang, Y. Lu, and C. Ning, J. Chem. Phys. **160**, 064303 (2024).
[11] S. Yan, R. Zhang, and C. Ning, J. Phys. Chem. Lett. **15**, 7735 (2024).
[12] J. Christoffersen, J. M. Hollas, and G. H. Kirby, Proc. R. Soc. London, Ser. A **307**, 97 (1968).
[13] T. E. H. Walker, P. M. Dehmer, and J. Berkowitz, J. Chem. Phys. **59**, 4292 (1973).
[14] F. Breyer, P. Frey, and H. Hotop, Z. Phys. A: Atoms Nucl. **300**, 7 (1981).
[15] P. A. Schulz, R. D. Mead, and W. C. Lineberger, Phys. Rev. A **27**, 2229 (1983).
[16] F. Goldfarb, C. Drag, W. Chaibi, S. Kröger, C. Blondel, and C. Delsart, J. Chem. Phys. **122**, 014308 (2005).
[17] J. P. Maillard, J. Chauville, and A. W. Mantz, J. Mol. Spectrosc. **63**, 120 (1976).
[18] R. Tang, X. Fu, and C. Ning, J. Chem. Phys. **149**, 134304 (2018).
[19] B. Dick, Phys. Chem. Chem. Phys. **16**, 570 (2014).
[20] B. Dick, Phys. Chem. Chem. Phys. **21**, 19499 (2019).
[21] L. D. Landau and E. M. Lifshitz, *Quantum Mechanics: Non-Relativistic Theory*, 3rd ed. (Pergamon Press, Oxford; New York, 1977), ISBN: 978-0-08-020940-1.
[22] I. Kovacs and W. Lichten, Phys. Today **25**(11), 54 (1972).
[23] A. Hansson and J. K. G. Watson, J. Mol. Spectrosc. **233**, 169 (2005).
[24] E. P. Wigner, Phys. Rev. **73**, 1002 (1948).
[25] J. T. Hougen, *The Calculation of Rotational Energy Levels and Rotational Line Intensities in Diatomic Molecules* (U.S. National Bureau of Standards, Washington, 1970), p. 15.
[26] H. Hotop, T. A. Patterson, and W. C. Lineberger, J. Chem. Phys. **60**, 1806 (1974).
[27] T. C. James and R. J. Thibault, J. Chem. Phys. **41**, 2806 (1964).
[28] J. D. Rudmin, L. P. Ratliff, J. N. Yukich, and D. J. Larson, J. Phys. B: At., Mol. Opt. Phys. **29**, L881 (1996).
[29] M. DeWitt, M. C. Babin, and D. M. Neumark, J. Phys. Chem. A **125**, 7260 (2021).
[30] R. Wild, M. Nötzold, M. Simpson, T. D. Tran, and R. Wester, Nature **615**, 425 (2023).
[31] J. R. Smith, J. B. Kim, and W. C. Lineberger, Phys. Rev. A **55**, 2036 (1997).
[32] H. W. Thompson and B. A. Green, Spectrochim. Acta **8**, 129 (1956).
[33] M. D. Olman, M. D. McNelis, and C. D. Hause, J. Mol. Spectrosc. **14**, 62 (1964).
[34] Y. Liu and C. Ning, J. Chem. Phys. **143**, 144310 (2015).
[35] R. S. da Silva, M. Y. Ballester, L. R. Ventura, and C. E. Fellows, Chem. Phys. Lett. **780**, 138896 (2021).
[36] J. W. C. Johns, J. Reid, and D. W. Lepard, J. Mol. Spectrosc. **65**, 155 (1977).
[37] D. B. Keck and C. D. Hause, J. Mol. Spectrosc. **26**, 163 (1968).
[38] J. W. C. Johns and D. W. Lepard, J. Mol. Spectrosc. **55**, 374 (1975).
[39] T. Amano and E. Hirota, J. Mol. Spectrosc. **53**, 346 (1974).
[40] W. H. Fletcher and J. S. Rayside, J. Raman Spectrosc. **2**, 3 (1974).
[41] M. W. Siegel, R. J. Celotta, J. L. Hall, J. Levine, and R. A. Bennett, Phys. Rev. A **6**, 607 (1972).
[42] M. J. Travers, D. C. Cowles, and G. B. Ellison, Chem. Phys. Lett. **164**, 449 (1989).
[43] D. T. Alle, M. J. Brennan, and S. J. Buckman, J. Phys. B: At., Mol. Opt. Phys. **29**, L277 (1996).
[44] C. A. Arrington, T. H. Dunning, and D. E. Woon, J. Phys. Chem. A **111**, 11185 (2007).
[45] D. Feller, J. Chem. Phys. **144**, 014105 (2016).
[46] J. L. Pack and A. V. Phelps, J. Chem. Phys. **44**, 1870 (1966).
[47] S. J. Nalley and R. N. Compton, Chem. Phys. Lett. **9**, 529 (1971).
[48] M. Allan, J. Phys. B: At., Mol. Opt. Phys. **28**, 5163 (1995).
[49] K. M. Ervin, I. Anusiewicz, P. Skurski, J. Simons, and W. C. Lineberger, J. Phys. Chem. A **107**, 8521 (2003).